Science of the Total Environment 615 (2018) 452–461

Contents lists available at ScienceDirect

Science of the Total Environment

journal homepage: www.elsevier.com/locate/scitotenv

Measurements of nonvolatile size distribution and its link to traffic soot in urban Shanghai

Shuqin Jiang [a], Xingnan Ye [a,b,*], Ruyu Wang [a], Ye Tao [a], Zhen Ma [a], Xin Yang [a,b], Jianmin Chen [a,b,*]

[a] Shanghai Key Laboratory of Atmospheric Particle Pollution and Prevention (LAP^3), Department of Environmental Science and Engineering, Fudan University, Shanghai 200433, China
[b] Institute of Atmospheric Sciences, Fudan University, Shanghai 200433, China.

HIGHLIGHTS

- Temporal variations of volatility shrink factor distribution is present.
- The concentration of nonvolatile mode particles is highly consistent with that of NO_x.
- The aerosol volatility is significantly different between haze and clean days.

GRAPHICAL ABSTRACT

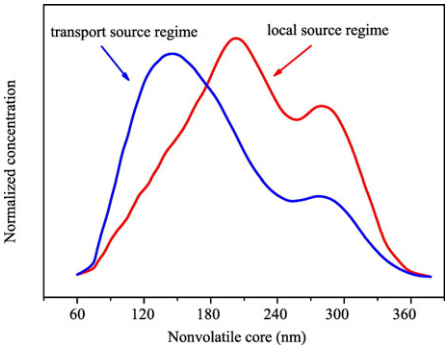

ARTICLE INFO

Article history:
Received 19 April 2017
Received in revised form 16 September 2017
Accepted 18 September 2017
Available online 5 October 2017

Editor: D. Barcelo

Keywords:
Nonvolatile particle
Volatility
Soot
Haze

ABSTRACT

Measurements of particle size distribution and size-resolved particle volatility were conducted using a volatility tandem differential mobility analyzers (V-TDMA) in the urban area of Shanghai during wintertime in January 2014. The nonvolatile mode particles with VSF exceeding 0.85 were always externally mixed with more-volatile mode particles. The average VSF ranged from 0.58 to 0.65 for 100–400 nm particles, increasing with the increase of particle size. On average, the nonvolatile mode contributed 15–20% of number fraction for 50–400 nm particles. Due to their hydrophobic nature, the nonvolatile particles were not easily removed by wet deposition. The concentrations of the nonvolatile mode particles and NO_x were well correlated, indicating that the nonvolatile mode particles were mostly attributed to be fresh traffic soot. The diurnal variations in ensemble VSF and number fraction of nonvolatile mode particles exhibited two peaks in clean days, corresponding to morning and evening rush hours. The VSF distributions of 50 nm particles were similar during a transition between haze to clean periods whereas in the accumulation mode range, the number fraction of more-volatile mode and the amount of volatile materials in the more-volatile mode particles during haze periods are considerably larger than those in clean periods, indicating different contribution from transported sources.

1. Introduction

Soot is produced from incomplete combustion of fossil fuel and biomass burning (Kondo et al., 2006). Once emitted into the atmosphere, soot particles gradually become internally mixed with a variety of chemical components through several atmospheric aging processes

* Corresponding authors at: Shanghai Key Laboratory of Atmospheric Particle Pollution and Prevention (LAP^3), Department of Environmental Science and Engineering, Fudan University, Shanghai 200433, China.
E-mail addresses: yexingnan@fudan.edu.cn (X. Ye), jmchen@fudan.edu.cn (J. Chen).

https://doi.org/10.1016/j.scitotenv.2017.09.176
0048-9697/

(Gong et al., 2016; Qiu et al., 2012; Riemer et al., 2004; Zuberi et al., 2005). After aging processes such as condensation, coagulation, oxidation, and cloud processing, the structure and mixing state of the soot particles are changed significantly (Chen et al., 2016; Ghazi and Olfert, 2013; Zhang et al., 2008).

Consisting mainly of black carbon and possibly coating with a thin layer of organic carbon, Soot particles are generally regarded as the most efficient light absorbing component of atmospheric aerosols (Bond and Bergstrom, 2006; Bond et al., 2013; Fierce et al., 2016; Rosen et al., 1978). After atmospheric aging with sulfate, nitrate, or organic carbon, the light absorbing capacity of internally mixed soot particles is quite distinct from the freshly emitted external mixture (Bond and Bergstrom, 2006). A nearly 2-fold enhancement on light absorption was observed after coating soot particles with sulfuric acid and subsequent hygroscopic growth at 80% RH (Zhang et al., 2008). It was suggested that soot was the second most important component of global warming after CO_2 in terms of direct forcing (Jacobson, 2001). Besides influence on their climate effects, the mixing state of soot particles also exists strong impact on atmospheric visibility. In urban area, traffic source is the major contribution of externally mixed soot particles whereas long-range transported soot particles are internally mixed with other particles or volatile compounds (Wehner et al., 2009). However, fresh soot particles are possibly modified to internally mixed in a very short time under the background of highly pollution (Gong et al., 2016).

To determine the mixing state of soot particles, V-TDMA was extensively employed both in laboratory research and field observations (Cheung et al., 2016; Sakurai et al., 2003; Wang et al., 2017; Wehner et al., 2009). After the pioneering work of Rader and McMurry (1986), Wehner et al. (2004) developed a V-TDMA that was capable of distinguishing volatile and non-volatile particles in the urban environment. On the basis of residual particle size distribution at temperature up to 300 °C, the V-TDMA can not only estimate the nonvolatile particle fraction of a selected monodisperse aerosol but also detect the thickness of volatile coating for the particles aged with a large amount of volatile substances.

Over the past 30 years, rapid industrialization and urbanization in China is accompanied with the increasing consumption of fossil-fuel such as coal, oil, and natural gas. A large amount of carbonaceous aerosols were emitted from power plant, daily traffic, industrial activities, and biomass burning, causing a significant impact on visibility, climate, and human health in China (Butt et al., 2016; Chen et al., 2017; Zhang et al., 2015). In this study, measurements of size-resolved aerosol volatility were conducted using a custom-built V-TDMA in the urban area of Shanghai during wintertime in January 2014. We present time-series of nonvolatile size distribution for 50–400 nm particles. Characteristics of aerosol volatility in clean and haze periods are discussed in detail. Also, the relations between nonvolatile mode particles and the concentrations of SO_2 and NO_x are investigated by comparing their temporal variations.

2. Experimental

2.1. Sampling site

The observation was deployed at the main campus of Fudan University (31.30°N, 121.5°E). There are many residential quarters and commercial blocks in the surrounding area. At 400 m south and 1000 m west of the measurement site, there are the Middle Ring Line and the Yixian Elevated Road, respectively, two of the busiest main roads in the city. Influenced with mixing pollutants emitted from traffic, residential, and industrial sources, the measurement site is a good representative of urban area in Shanghai.

2.2. Volatility measurements

The volatility measurement was conducted from January 1 to 20, 2014 in the Environmental Building in the school using the custom-built V-TDMA. The ambient aerosol was pumped into the laboratory at 10 l min^{-1} through a main sampling tube with an inner diameter of 1/2 in. The inlet of the sampling tube was about 1 m above the roof of the building. A 0.4 l min^{-1} aerosol sample was bypassed at the end of the main sampling tube and introduced into the V-TDMA through a 1.5 m long Swagelok® stainless steel tube with a 1/4 in diameter.

The V-TDMA was upgraded from our custom-built hygroscopic-TDMA described previously in detail (Ye et al., 2009). In the V-TDMA (Fig. 1), the heat denuder is located between the upstream and downstream DMAs (Model 3081 L, TSI Inc.) instead of the humidifier in the hygroscopic TDMA. Briefly, the aerosol sample was dried at RH < 20% (determined by the RH sensor before the Condensation Particle Counter (CPC, Model 3771, TSI Inc.)) before charging and subsequently entering the upstream DMA1. The V-TDMA was operated alternatively in SMPS mode and then V-TDMA mode. In the SMPS mode, particle size distribution in the range of 14–600 nm dry diameter was determined. In the V-TDMA mode, the monodisperse aerosols with dry mobility diameters of 50, 100, 200, 300, and 400 nm were selected and then sent to the heat denuder at 300 °C in turn. The residence time of the selected aerosols in the heating zone of the denuder is about 1.5 s. Finally, the residual aerosols after evaporation at 300 °C were screened by the downstream DMA2 to obtain the nonvolatile size distribution. The volatility shrink factor (VSF) is defined as relative decrease in mobility diameter of dry particles due to evaporation at a certain temperature:

$$VSF = \frac{D_T}{D_0}$$

where D_T is the mobility diameter of residual particles after heating at a specific temperature T, and D_0 is the initial dry particle mobility diameter of the selected monodisperse aerosol.

2.3. Measurements of air quality index and meteorological parameters

The meteorological parameters (e. g., ambient temperature, relative humidity, wind direction and speed, and precipitation) were continuously measured by an automatic meteorological station (Model CAWS600, Huayun Inc., China) equipped with a Model HMP155 temperature and RH sensor. The data about air pollutants (e. g. the hourly concentrations of $PM_{2.5}$, SO_2, and NO_x) were provided by the Pudong Area Monitoring Station of the Shanghai Environmental Monitoring Center, a distance of ~8 km to the main campus of Fudan University.

3. Results and discussion

3.1. Overviews of meteorological conditions

Located at the estuary of the Yangtze River, Shanghai has a subtropical monsoon climate with the prevailing wind directions typically from northwest to northeast in the winter and from southeast to southwest in the summer (Chan and Yao, 2008). Fig. 2 shows the main meteorological parameters during the observation. The ambient temperature (T) and relative humidity (RH) displayed obvious diurnal cycle patterns,

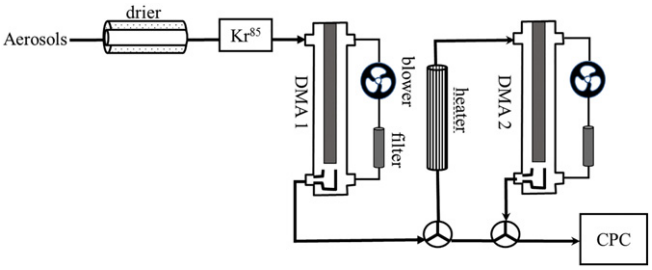

Fig. 1. A schematic plot of the custom-built Volatility-TDMA system.

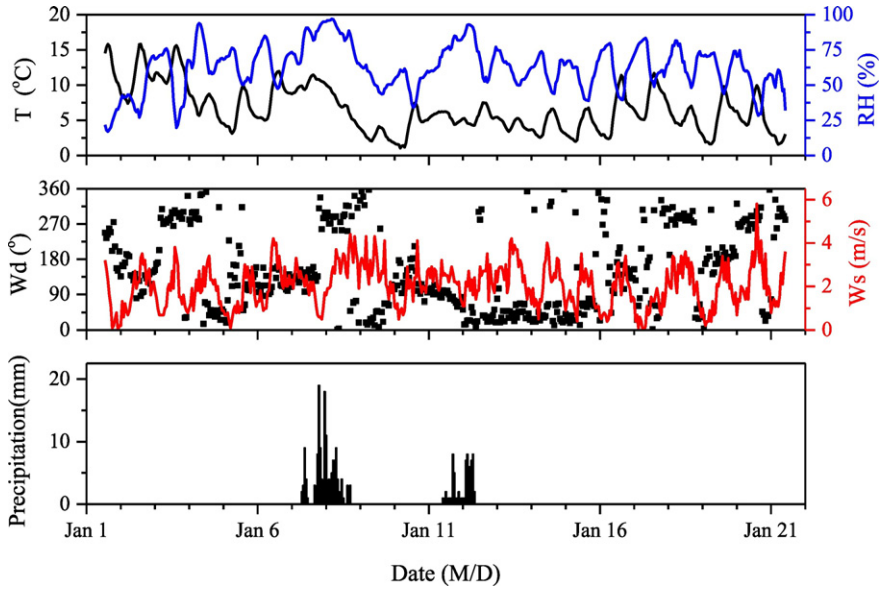

Fig. 2. Meteorological conditions during the observation.

except during rainy days. The average temperature was 6.6 ± 2.3 °C, with the highest hourly temperature over 15 °C for 3 days and the lowest hourly temperature below 3 °C for 6 days. Generally, January is the coldest month of the year in Shanghai. However, the ambient temperature did not drop to 0 °C during the whole observation, indicating a warmer winter which favored the accumulation of particulate pollutants and transformation of their gas precursors. The prevailing winds were northerly, consistent with the typical climate characteristics of Shanghai. The average wind speed was 2.03 ± 0.97 m s^{-1}. The wind speed also displayed a clear diurnal cycle pattern. Except during rainy days, the wind speed increased in the early morning and reached a maximum at noontime, and then it decreased slowly until midnight. The removal of primary emissions was suppressed during nighttime due to the formation of planetary boundary layer (PBL) and the decrease in wind speed until the next morning when a well boundary layer and higher wind speed favored atmospheric dilution. There were two rainfall periods during the observation with a total precipitation of 153 mm. The wet precipitation can remove gas pollutants and aerosol particles effectively, which mitigates effectively air pollution in Shanghai.

3.2. Temporal variations of particle size distribution over the observation period

Fig. 3 displays the temporal evolution of particle number distribution along with the $PM_{2.5}$ (particulate matter smaller than 2.5 μm in aerodynamic diameter) mass concentration during the observation period. Referring to the average effective density of 1.39 g m^{-3}

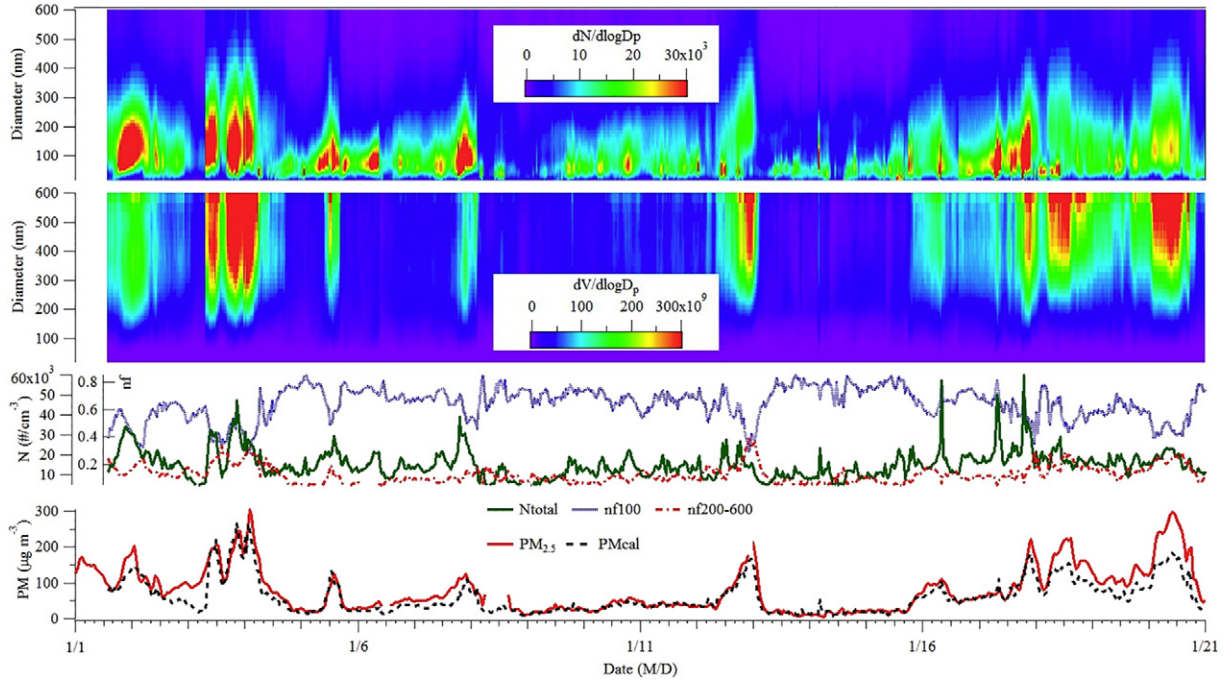

Fig. 3. Time-series of particle size distribution in comparison with $PM_{2.5}$ concentration during the observation. Ntotal: the number concentration of the particles in the range of 15–600 nm; nf100 and nf200–600 are number fraction of the particles below 100 nm and in the range of 200–600 nm, respectively.

determined in a previous study (Xie et al., 2017), the particulate mass concentration in the range of 15–600 nm in mobility diameter was calculated and expressed as PM_{cal}. Although there were two rainfall processes and considerably high wind speeds, the average concentration of $PM_{2.5}$ was as high as 79.5 ± 60.3 μg m^{-3} over the 20-day observation, indicating severe fine particulate pollution in winter. Two distinct haze events occurred in the periods of January 1 to 4 (Haze I) and January 17 to 20 (Haze II). The daily-averaged $PM_{2.5}$ concentration was below the Chinese Grade-II standards (75 μg m^{-3} for 24 h average, GB 3095-2012) in other days, except on January 12 when a brief haze event burst out. Different from periodic PM episodes in Chinese megacities reported previously (Guo et al., 2014; Wang et al., 2016; Xie et al., 2017), the air quality was acceptable in most of the days in the current study, possibly because the accumulation of local emissions was suspended by the diurnal cycle of wind speed.

The concentration of the particles in the range of 15–600 nm varied from below 5000 to larger than 60,000 particles cm^{-3} during the observation period. The temporal trend of $PM_{2.5}$ mass loading was similar to that of particle number concentration during the period of Haze I whereas they displayed different patterns during the period of Haze II, indicating that $PM_{2.5}$ mass loading was not closely correlated with the number of the particles. It is noticeable that the particle size distribution was dominated by nanoparticles (below 100 nm in diameter) during clean periods whereas the number fraction of nanoparticles decreased considerably with the increase of $PM_{2.5}$ mass concentration during the haze periods. In contrast, the number fraction of the particles larger than 200 nm increased significantly as the PM episodes developed. This finding indicates that the elevated particle mass was attributable to the presence of numerous larger particles. However, the particle growth process was not observed in this campaign, suggesting that the condensation growth was not responsible for the presence of numerous larger particles.

Regardless of different size ranges between $PM_{2.5}$ and $PM_{cal,}$ there were smaller difference between the concentration of $PM_{2.5}$ and PM_{cal} except during Haze II, possibly due to the following reasons: 1) They were measured in different sites; 2). There existed very few particles larger than 600 nm in mobility diameter.

3.3. Temporal variation of size-fractioned volatility during the observation

Fig. 4 displays time-series of VSF distribution for different sizes during the observation. The inserted red line represents the ensemble VSF. After heating at 300°C, the secondarily produced SNA (sulfate, nitrate, and ammonium) and most of the organic species were evaporated, implying that the residual nonvolatile materials mostly consisted of soot, sea salt, and soil dust. In urban areas and for the submicrometer range, the majority of the nonvolatile particle mass can be assumed to be soot (Wehner et al., 2009). In this study, the measured nonvolatile size distribution after heating at 300 °C is expressed as VSF distribution by dividing the residual size with the initial diameter. For the particles of one selected diameter, most of the VSF distributions were apparently bimodal. The mean VSF of the first peak was approximately equal to unity, indicating that these particles were almost non-volatile. We attribute the nonvolatile group to fresh soot, because the soot particles become more volatile during atmospheric aging due to continuous coating of volatile materials on the soot surface. Considering that the ratio of sheath flow and sample flow in the V-TDMA was set as 7.5, particles with VSF > 0.85 at 300 °C are assumed to be externally mixed nonvolatile mode particles while particles with VSF < 0.85 at 300 °C are attributed to more-volatile mode. The number fraction of the nonvolatile group varied considerably, depending on both primary emissions and atmospheric conditions. The secondary peak broadened and shift to a lower VSF, indicative of aged soot internally mixed with volatile materials. This finding indicates that the selected monodisperse aerosol of a certain size consisted of different fractions of nonvolatile materials (Wehner et al., 2009). The 50 nm particle population had the smallest average VSF of 0.58 ± 0.05, ranging between 0.79 and 0.45 over the observation period. For accumulation mode particles, the average VSFs were 0.60 ± 0.04, 0.60 ± 0.05, 0.61 ± 0.06, and 0.65 ± 0.06 for 100, 200, 300, and 400 nm particles, respectively. Generally, the average volatility shrink factor increased with particle size, indicating that particle volatility decreased with the increase of particle size. This finding demonstrates that the presence of numerous larger accumulation particles could not be attributable to condensation growth of smaller Aitken mode particles, because the condensation of secondary vapors will

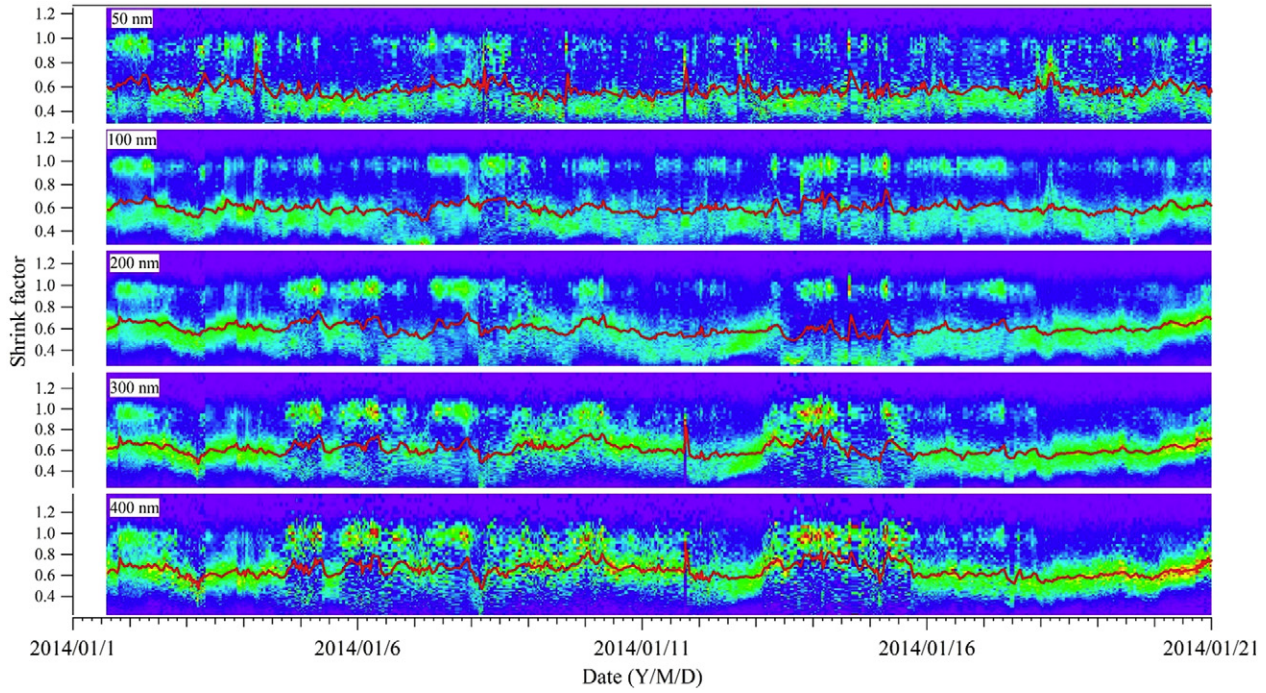

Fig. 4. Time-series of volatility shrink factor distribution for different sizes during the observation. The inserted red curve represents the ensemble volatility shrink factor.

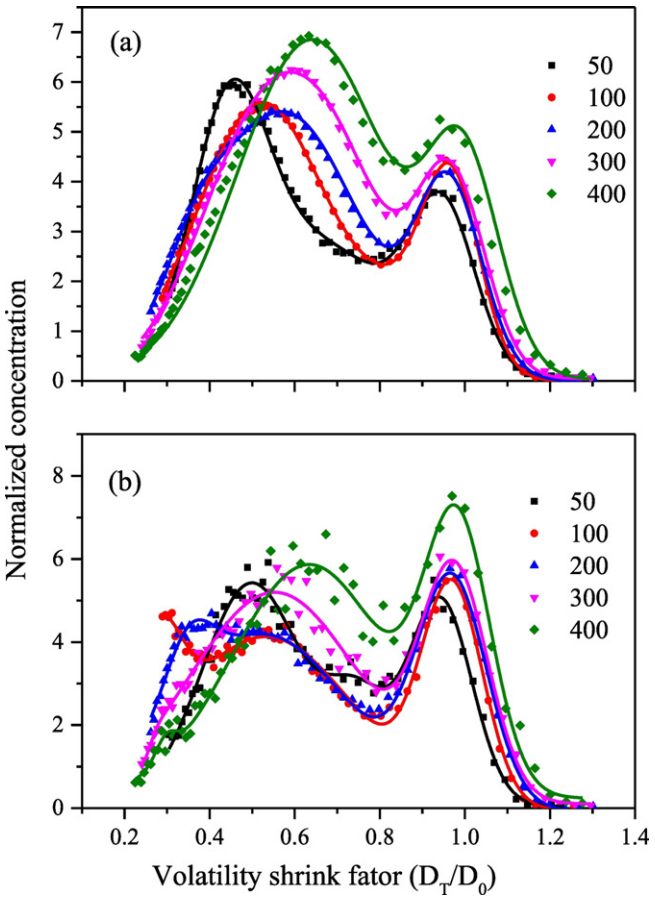

Fig. 5. Average volatility shrink factor distributions for different sizes during (a) the whole observation and (b) rain days.

increase particle volatility. A similar feature was found in Beijing (Wang et al., 2017). In contrast, Levy et al. (2014) reported an opposite trend in Tijuana, Mexico that the volatile fraction of submicron aerosols increased with particle size. This finding indicates that the sources and chemical components of atmospheric particles vary from region to region.

3.4. Size-dependent volatility shrink factor distribution

Fig. 5 illustrates the observation-averaged VSF distribution for different sizes, along with those in rainy days. The lower limit of VSF distribution varied in the range of 0.2–0.3, depending on initial particle size. The lower limit of VSF distribution was set as 0.3 for 50 nm particles, because the lower detect limit of the V-TDMA is 14.7 nm. All sizes displayed a bimodal distribution with one peak near 1.0 and another broad and asymmetric peak between 0.45 and 0.65. For 50 nm particles, the two modes peaked at 0.93 and 0.46. For 100 to 400 nm particles, the nonvolatile mode particles exhibited similar VSF for different initial sizes. In contrast, the mode peak of the more-volatile mode group varied with initial particle size. Interestingly, the more-volatile mode peaked at 0.52, 0.57, 0.59, and 0.63 for 100, 200, 300, and 400 nm particles, indicating that volatility decreased with the increase in particle size. This finding is consistent with the result of field campaigns in Beijing (Wang et al., 2017; Wehner et al., 2009), but inconsistent with those measured in Tijuana, Mexico (Levy et al., 2014). Wehner et al. (2009) divided the more-volatile group into medium-volatile and high-volatile subgroups and found that the number fraction of medium-volatile group increased with the increase of particle size during less polluted periods, which indicates that the mean VSF of the more-volatile group increased with particle size. For more-volatile mode, the nonvolatile core increased from 23 nm for 50 nm particles to 252 nm for 400 nm particles. This finding further supports the aforementioned conclusion that the presence of larger accumulation mode particles cannot be explained by condensation growth of smaller Aitken mode particles. The nonvolatile mode particles contributed 15–20% of number fraction for 50–400 nm particles, increasing with particle size. We should point out that the nonvolatile mode fractions may be overestimated, particularly for 50 nm particles, because the diameters of some nonvolatile cores after heating at 300 °C might be below the default detect limit of the V-TDMA. The systematic error decreased with the increase of initial particle size and was negligible for 400 nm particles, because the concentration of residuals with the diameter equal to the detect limit was close to zero.

During rainy days, the volatility of volatile mode particles in diameters of 300 and 400 nm was similar to those in other days. The 100 and 200 nm particles exhibited the third volatile mode, possibly coated with larger amounts of insoluble organics. It is noticeable that the nonvolatile particles in rainy days contributed 19–27% of number fraction for 50–400 nm particles, considerably higher than the observation-averaged values. The most plausible explanation is that the nonvolatile particles are very hydrophobic so that the precipitation scavenging is extremely inefficient for them. Kondo et al., 2006 estimated that the time constant for the removal of Aitken and smaller accumulation mode hydrophobic particles by falling raindrops was longer than 4 days. In contrast, the more-volatile particles with coating of inorganic species can be easily removed by rainout due to their hygroscopic nature.

3.5. Traffic influence on the concentration of nonvolatile particles

As an important type of primary particles in urban area, soot is a product of incomplete biomass burning and fossil fuel combustion in vehicle traffic and industrial activities. To identify the source origin of the nonvolatile mode particles, the temporal variation of number concentration of nonvolatile particles was compared with mass concentrations of NO_x and SO_2 in Fig. 6, because NO_x is mainly produced from local traffic emissions in urban area and it is used as an indicator of traffic (Levy et al., 2013; Rissler et al., 2014) whereas the pollution level of SO_2 was significantly influenced by reginal transport (Guo et al., 2014). Additional correlation analysis among them is illustrated in Fig. 7. The concentrations of the nonvolatile mode particles and NO_x were well correlated ($R^2 = 0.61$) over the observation period, indicating that they were of the same source origin. In contrast, the concentration of SO_2 varied in a different pattern from those of NO_x and nonvolatile particles ($R^2 = 0.09$), indicating significant contribution of long-range or reginal transports. This finding reveals that the nonvolatile particles were mostly attributable to fresh soot of traffic source. The diurnal variation of NO_x and nonvolatile particles usually display two rush-hour peaks, thus further supporting their traffic source. However, the peak concentration of NO_x fluctuated widely from day to day, due to strong impact of meteorological conditions.

3.6. Diurnal variation of aerosol volatility in clean and haze periods

Fig. 8 compares the diurnal variations of aerosol volatility during clean and haze periods. Considering that the $PM_{2.5}$ concentration dropped rapidly and it was lower than 75 μg m^{-3} from 12:00, we excluded the data measured on January 4 from the statistical average of haze periods. To avoid the influence from precipitation scavenging, all data measured in rainy days were also excluded from the clean periods. The ensemble VSF and the number fraction of nonvolatile particles displayed similar variation patterns, indicating that the change in ensemble VSF was dominated by the relative contribution of the two volatility modes rather than by the volatility of the more-volatile mode. This finding suggests that traffic emission imposed significant impact on the ensemble VSF.

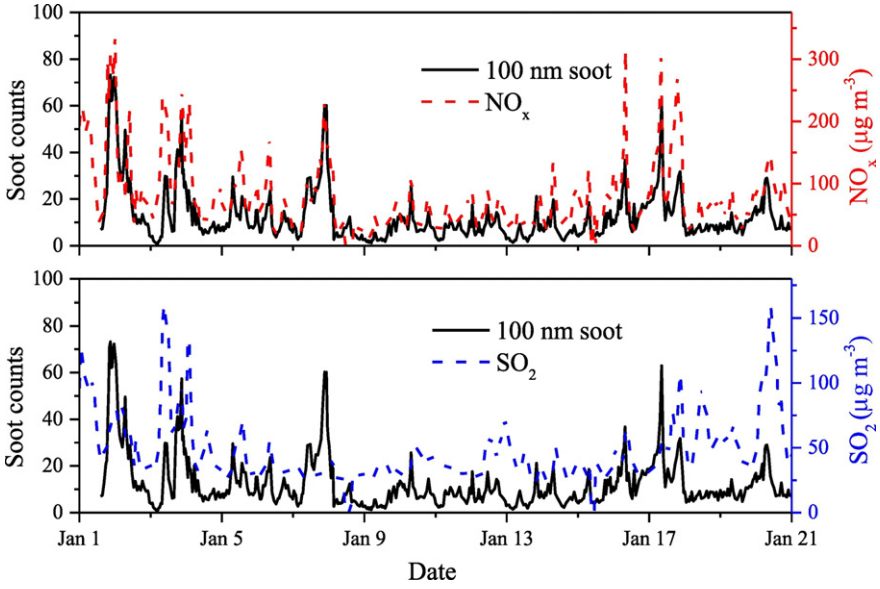

Fig. 6. Time-series of the concentration of fresh soot, along with the concentrations of NO_x and SO_2 during the observation.

During the clean periods, the ensemble VSF increased from 6:00 in the early morning and reached a maximum at 8:00. The morning traffic continued from 6:00 to 10:00 in Shanghai. The increase in ensemble VSF was consistent with the increase of on-road traffic flow, indicating that the morning peak in the diurnal trend of the ensemble VSF was attributable to morning traffic. The ensemble VSF decreased before the end of rush hour, possibly because the atmospheric dilution was strengthened due to the development of PBL as well as coating of secondary aerosols on the soot particles due to photo-chemical reactions. The minimum ensemble VSF appeared at noon time, corresponding to the highest PBL and the lowest traffic during daytime. The diurnal variation of ensemble VSF exhibited another peak at evening rush hour for all sizes. However, the evening peaks were less significant than those morning ones except for 50 nm particles, possibly due to the comprehensive effect of various factors. First, the traffic volume during the evening rush hour increased more slowly than that in the morning; secondly, a large amount of aged particles formed in the daytime decreased the number fraction of non-volatile particles during the evening rush hour. The ensemble VSF remained relatively high overnight, due to couple effect of atmospheric accumulation and heavy diesel trucks. It was reported that the soot emission factor of diesel vehicles was about five times as that of gasoline vehicles (Jezek et al., 2015).

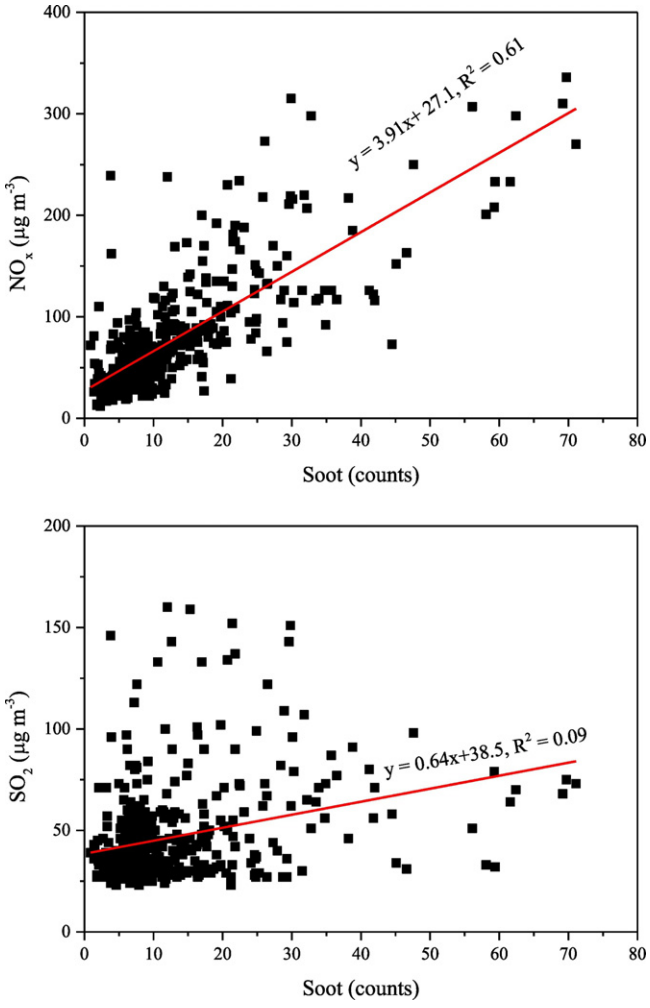

Fig. 7. The concentrations of NO_x and SO_2 as a function of the concentration of fresh soot during the observation period.

During the haze periods, the diurnal variation of ensemble VSF for 50 nm particles also exhibited two rush-hour peaks whereas the intensity of evening peak was decreased. In addition, the concentration of background aerosols increased considerably, which decreased the relative contribution of fresh emissions to the total particles. The presence of rush-hour peak indicates strong traffic emissions in urban Shanghai. During haze periods, the morning VSF peaks of accumulation mode particles were smaller and delayed with the increase of particle size. These features can be partly explained by the size distribution of gasoline exhausts. It was reported that the median diameter of traffic particles from gasoline sources ranged between 55 and 73 nm with an average of 65 nm (Momenimovahed and Olfert, 2015). The delayed peak for accumulation particles is possibly related to rapid particle growth during the haze periods.

3.7. Influence of air masses on the aerosol volatility under similar meteorological conditions

As shown in Fig. 3, the short haze on Jan 12 occurred just after a precipitation and disappeared in <24 h. The precipitation began at 10:00 on Jan 11 and continued until 8:00 on Jan 12 (Fig. 1). The average $PM_{2.5}$ concentration was $37 \pm 4\ \mu g\ m^{-3}$ during the rainy period, with the lowest concentration of $27\ \mu g\ m^{-3}$ at the end. After the rain, the $PM_{2.5}$ mass

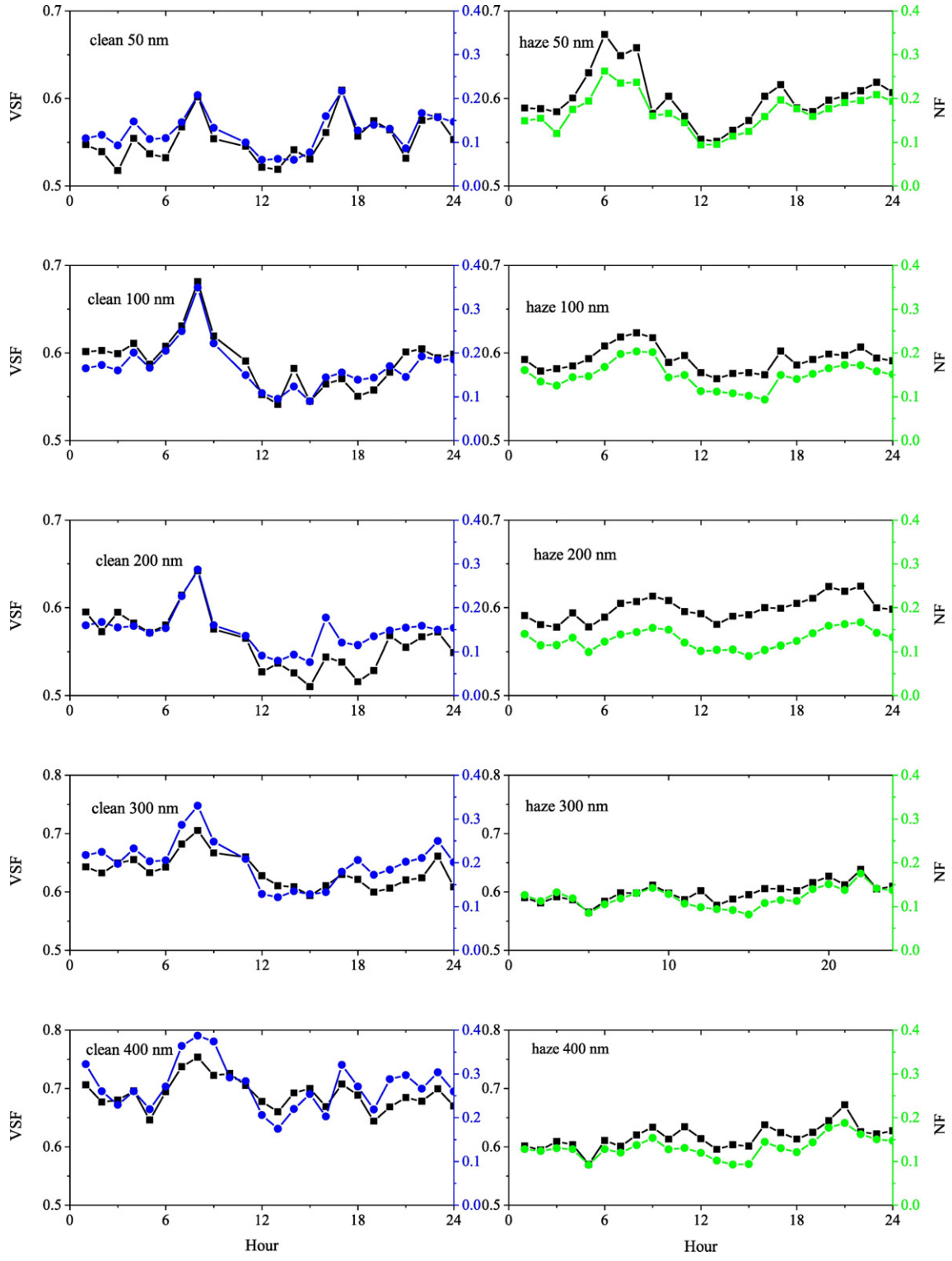

Fig. 8. Diurnal variations of ensemble volatility shrink factor and number fraction of non-volatile mode particles between clean and haze periods.

climbed up to 75 μg m^{-3} within 4 h and maintained over 100 μg m^{-3} from 16:00 on Jan 12 to 2:00 on Jan 13. Then, the air quality improved rapidly and the $PM_{2.5}$ mass decreased to <25 μg m^{-3} within 3 h. Interestingly, no significant change in the main meteorological parameters (e.g., wind direction and speed, temperature and relative humidity) was found during the transition of pollution level.

Fig. 9 compares the average VSF distributions on Jan 12 (haze) and Jan 13 (clean) for different sizes. Although the pollution levels were considerably different, the average VSF distributions for 50 nm particles were almost identical in these two days. This feature indicates similar sources of these Aitken mode particles. Laakso et al. (2003) suggested that nucleation and Aitken mode particles in urban areas came from local sources and especially from traffic source whereas long-range transport contributed to accumulation mode particles. In contrast, the average VSF distributions of accumulation mode particles were completely different between the haze and clean days. It is noticeable

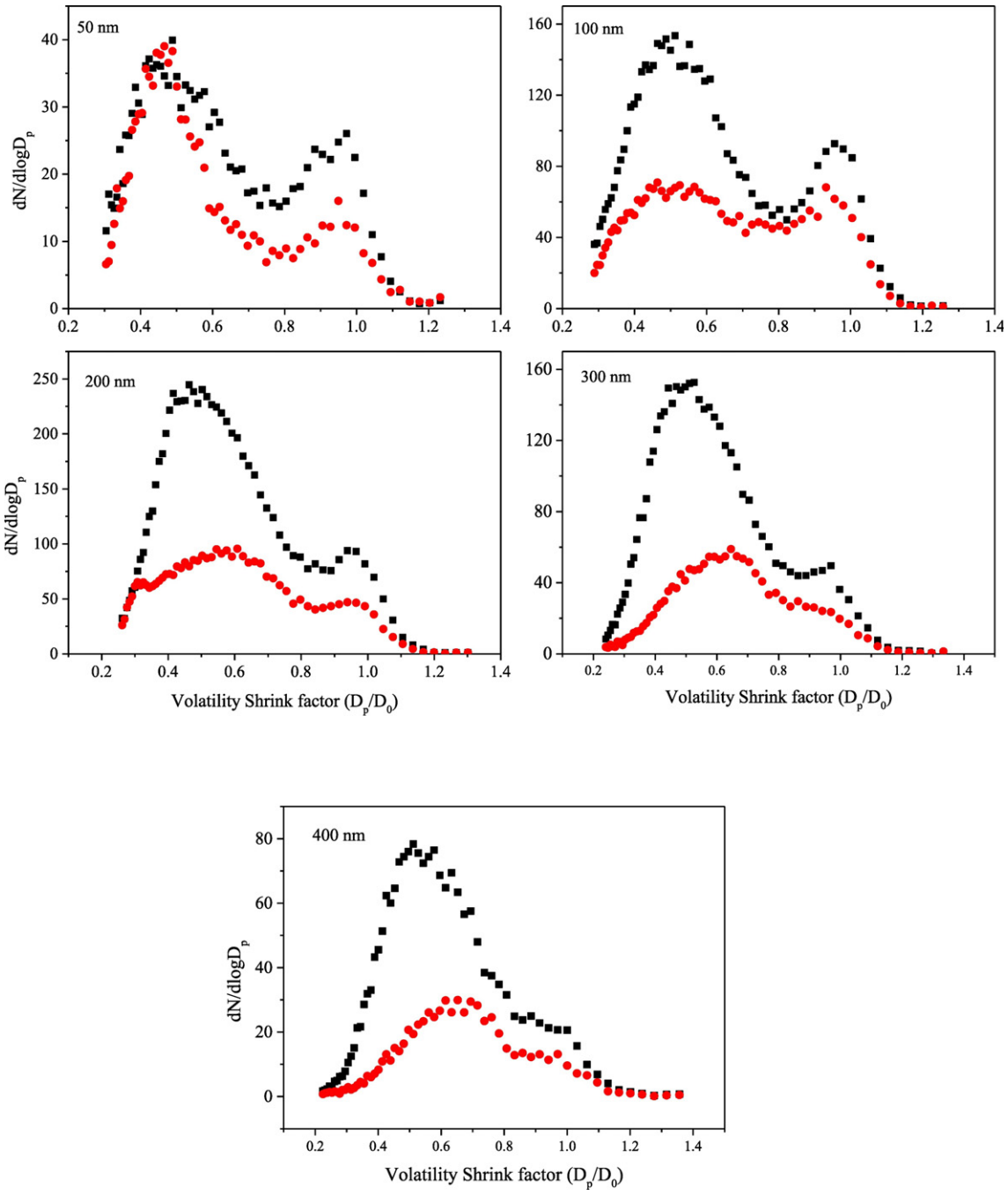

Fig. 9. Comparisons of shrink factor distributions during a transition period under similar meteorological conditions. (■) Jan 12; (●) Jan 13.

that both the concentration and number fraction of the more-volatile particles on Jan 12 were considerably higher than those on Jan 13 for 100–400 nm particles, indicating elevated concentrations of highly aged accumulation mode particles. Meanwhile, the more-volatile mode VSFs on Jan 12 were smaller than those on Jan 13, indicating larger fractions of volatile materials. Being mixed with pollutants along the way, the long-range transported aerosols became more aged and more volatile due to secondary formation and condensation growth. These features indicate larger contribution of long-range transport to $PM_{2.5}$ during the period of the short haze.

To explain the different contributions of long-range transport under similar wind direction and speed, air masses arriving in Shanghai were identified by the HYSPLIT model on web (Stein et al., 2015). As shown in Fig. 10, the back-trajectories of the air masses at 500 m high show that the air masses originated from China inland first moved towards the southeast and then turned southerly over the Yellow Sea before arriving Shanghai on Jan 12. The air masses were transported over the polluted areas in Hebei and Shandong provinces at lower altitudes (below 1000 m), indicating highly aged aerosols. In contrast, the air masses arriving in Shanghai on Jan 13 originated from the above 3000 m upper atmosphere over Siberia and passed by the upper atmosphere along the way before arriving in Shanghai, which favored the dilution of the urban emissions with clean air.

4. Conclusions

The size-resolved mixing state of nonvolatile particles was determined in Shanghai using a custom-built Volatility TDMA on January 2014.

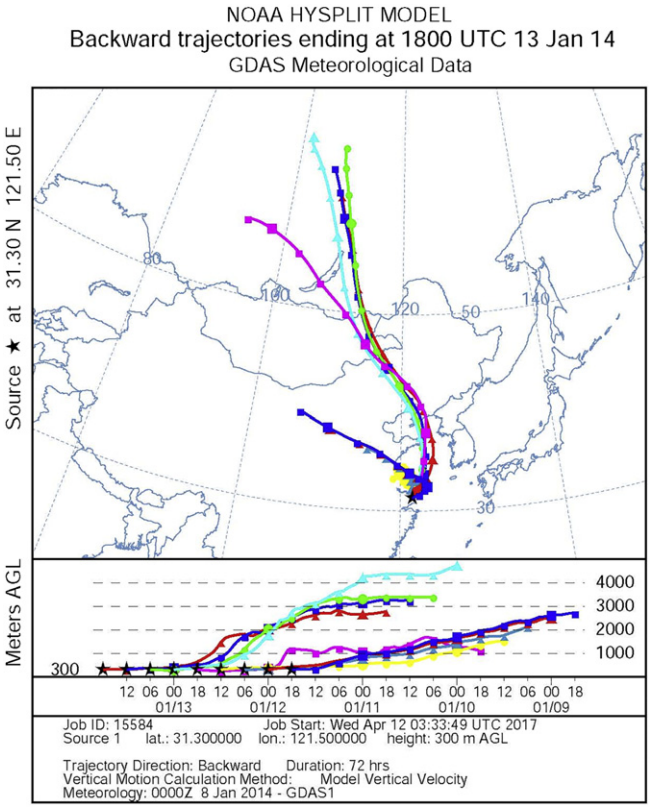

Fig. 10. 72 h back-trajectories arriving in Shanghai in the period of January 12 to 13.

Two typical haze episodes and a short haze event occurred during the observation whereas the air quality was acceptable in other days. The particle size distribution was dominated by nanoparticles during clean periods whereas the particles larger than 200 nm increased significantly as the PM episodes developed.

Most of the VSF distributions were bimodal, consisting of externally and internally mixed nonvolatile particles. Both volatility of the more-volatile mode particles and the ensemble volatility of a certain diameter decreased with the increase of particle size, indicating that the presence of numerous larger particles could not be attributable to condensation growth of smaller Aitken mode particles. The number fraction of non-volatile mode particles was considerably increased in rainy days, because the precipitation scavenging of nonvolatile mode particles is extremely inefficient due to their hydrophobic nature.

The ensemble VSF and the number fraction of nonvolatile mode particles displayed similar variation patterns, indicating that traffic soot imposed significant impact on the ensemble VSF. The presence of two peaks in the diurnal variation profile of VSF were attributed to the morning and evening rush-hour traffics. The rush-hour peak was less significant during haze periods because the concentration of background aerosols was highly enhanced. A short haze and a very clean day were present in sequence under similar meteorological conditions. Back-trajectories show that the short haze was attributable to the long-range transported air masses from polluted area while the improvement of atmospheric diffusion conditions was responsible for the clean sky in the next day.

Acknowledgments

This work was supported by the National Natural Science Foundation of China (21477020, 21527814, and 91544224), and the National Science and Technology Support Program of China (2014BAC22B01). The authors gratefully acknowledge the NOAA Air Resources Laboratory (ARL) for the provision of the HYSPLIT transport and dispersion model used in this publication.

References

Bond, T.C., Bergstrom, R.W., 2006. Light absorption by carbonaceous particles: an investigative review. Aerosol Sci. Technol. 40, 27–67.
Bond, T.C., Doherty, S.J., Fahey, D.W., Forster, P.M., Berntsen, T., DeAngelo, B.J., Flanner, M.G., Ghan, S., Kaercher, B., Koch, D., Kinne, S., Kondo, Y., Quinn, P.K., Sarofim, M.C., Schultz, M.G., Schulz, M., Venkataraman, C., Zhang, H., Zhang, S., Bellouin, N., Guttikunda, S.K., Hopke, P.K., Jacobson, M.Z., Kaiser, J.W., Klimont, Z., Lohmann, U., Schwarz, J.P., Shindell, D., Storelvmo, T., Warren, S.G., Zender, C.S., 2013. Bounding the role of black carbon in the climate system: a scientific assessment. J. Geophys. Res.-Atmos. 118, 5380–5552.
Butt, E.W., Rap, A., Schmidt, A., Scott, C.E., Pringle, K.J., Reddington, C.L., Richards, N.A.D., Woodhouse, M.T., Ramirez-Villegas, J., Yang, H., Vakkari, V., Stone, E.A., Rupakheti, M., Praveen, P.S., van Zyl, P.G., Beukes, J.P., Josipovic, M., Mitchell, E.J.S., Sallu, S.M., Forster, P.M., Spracklen, D.V., 2016. The impact of residential combustion emissions on atmospheric aerosol, human health, and climate. Atmos. Chem. Phys. 16, 873–905.
Chan, C.K., Yao, X., 2008. Air pollution in mega cities in China. Atmos. Environ. 42, 1–42.
Chen, C., Fan, X., Shaltout, T., Qiu, C., Ma, Y., Goldman, A., Khalizov, A.F., 2016. An unexpected restructuring of combustion soot aggregates by subnanometer coatings of polycyclic aromatic hydrocarbons. Geophys. Res. Lett. 43, 11080–11088.
Chen, J.M., Li, C.L., Ristovski, Z., Milic, A., Gu, Y.T., Islam, M.S., Wang, S.X., Hao, J.M., Zhang, H.F., He, C.R., Guo, H., Fu, H.B., Miljevic, B., Morawska, L., Thai, P., Fat, L., Pereira, G., Ding, A.J., Huang, X., Dumka, U.C., 2017. A review of biomass burning: emissions and impacts on air quality, health and climate in China. Sci. Total Environ. 579, 1000–1034.
Cheung, H.H.Y., Tan, H., Xu, H., Li, F., Wu, C., Yu, J.Z., Chan, C.K., 2016. Measurements of non-volatile aerosols with a VTDMA and their correlations with carbonaceous aerosols in Guangzhou, China. Atmos. Chem. Phys. 16, 8431–8446.
Fierce, L., Bond, T.C., Bauer, S.E., Mena, F., Riemer, N., 2016. Black carbon absorption at the global scale is affected by particle-scale diversity in composition. Nat. Commun. 7.
Ghazi, R., Olfert, J.S., 2013. Coating mass dependence of soot aggregate restructuring due to coatings of oleic acid and dioctyl sebacate. Aerosol Sci. Technol. 47, 192–200.
Gong, X., Zhang, C., Chen, H., Nizkorodov, S.A., Chen, J., Yang, X., 2016. Size distribution and mixing state of black carbon particles during a heavy air pollution episode in Shanghai. Atmos. Chem. Phys. 16, 5399–5411.
Guo, S., Hu, M., Zamora, M.L., Peng, J., Shang, D., Zheng, J., Du, Z., Wu, Z., Shao, M., Zeng, L., Molina, M.J., Zhang, R., 2014. Elucidating severe urban haze formation in China. Proc. Natl. Acad. Sci. U. S. A. 111, 17373–17378.
Jacobson, M.Z., 2001. Strong radiative heating due to the mixing state of black carbon in atmospheric aerosols. Nature 409, 695–697.
Jezek, I., Katrasnik, T., Westerdahl, D., Mocnik, G., 2015. Black carbon, particle number concentration and nitrogen oxide emission factors of random in-use vehicles measured with the on-road chasing method. Atmos. Chem. Phys. 15, 11011–11026.
Kondo, Y., Komazaki, Y., Miyazaki, Y., Moteki, N., Takegawa, N., Kodama, D., Deguchi, S., Nogami, M., Fukuda, M., Miyakawa, T., Morino, Y., Koike, M., Sakurai, H., Ehara, K., 2006. Temporal variations of elemental carbon in Tokyo. J. Geophys. Res.-Atmos. 111.
Laakso, L., Hussein, T., Aarnio, P., Komppula, M., Hiltunen, V., Viisanen, Y., Kulmala, M., 2003. Diurnal and annual characteristics of particle mass and number concentrations in urban, rural and Arctic environments in Finland. Atmos. Environ. 37, 2629–2641.
Levy, M.E., Zhang, R.Y., Khalizov, A.F., Zheng, J., Collins, D.R., Glen, C.R., Wang, Y., Yu, X.Y., Luke, W., Jayne, J.T., Olaguer, E., 2013. Measurements of submicron aerosols in Houston, Texas during the 2009 SHARP field campaign. J. Geophys. Res.-Atmos. 118, 10518–10534.
Levy, M.E., Zhang, R.Y., Zheng, J., Tan, H.B., Wang, Y., Molina, L.T., Takahama, S., Russell, L.M., Li, G.H., 2014. Measurements of submicron aerosols at the California-Mexico border during the Cal-Mex 2010 field campaign. Atmos. Environ. 88, 308–319.
Momenimovahed, A., Olfert, J.S., 2015. Effective density and volatility of particles emitted from gasoline direct injection vehicles and implications for particle mass measurement. Aerosol Sci. Technol. 49, 1051–1062.
Qiu, C., Khalizov, A.F., Zhang, R., 2012. Soot aging from OH-initiated oxidation of toluene. Environ. Sci. Technol. 46, 9464–9472.
Rader, D.J., McMurry, P.H., 1986. Application of the tandem differential mobility analyzer to studies of droplet growth or evaporation. J. Aerosol Sci. 17, 771–787.
Riemer, N., Vogel, H., Vogel, B., 2004. Soot aging time scales in polluted regions during day and night. Atmos. Chem. Phys. 4, 1885–1893.
Rissler, J., Nordin, E.Z., Eriksson, A.C., Nilsson, P.T., Frosch, M., Sporre, M.K., Wierzbicka, A., Svenningsson, B., Londahl, J., Messing, M.E., Sjogren, S., Hemmingsen, J.G., Loft, S., Pagels, J.H., Swietlicki, E., 2014. Effective density and mixing state of aerosol particles in a near-traffic urban environment. Environ. Sci. Technol. 48, 6300–6308.
Rosen, H., Hansen, A.D.A., Gundel, L., Novakov, T., 1978. Identification of optically absorbing component in urban aerosols. Appl. Opt. 17, 3859–3861.
Sakurai, H., Park, K., McMurry, P.H., Zarling, D.D., Kittelson, D.B., Ziemann, P.J., 2003. Size-dependent mixing characteristics of volatile and nonvolatile components in diesel exhaust aerosols. Environ. Sci. Technol. 37, 5487–5495.
Stein, A.F., Draxler, R.R., Rolph, G.D., Stunder, B.J.B., Cohen, M.D., Ngan, F., 2015. NOAA's HYSPLIT atmospheric transport and dispersion modeling system. Bull. Am. Meteorol. Soc. 96, 2059–2077.
Wang, G., Zhang, R., Gomez, M.E., Yang, L., Zamora, M.L., Hu, M., Lin, Y., Peng, J., Guo, S., Meng, J., Li, J., Cheng, C., Hu, T., Ren, Y., Wang, Y., Gao, J., Cao, J., An, Z., Zhou, W., Li, G., Wang, J., Tian, P., Marrero-Ortiz, W., Secrest, J., Du, Z., Zheng, J., Shang, D., Zeng, L., Shao, M., Wang, W., Huang, Y., Wang, Y., Zhu, Y., Li, Y., Hu, J., Pan, B., Cai, L., Cheng, Y., Ji, Y., Zhang, F., Rosenfeld, D., Liss, P.S., Duce, R.A., Kolb, C.E., Molina, M.J.,

2016. Persistent sulfate formation from London fog to Chinese haze. Proc. Natl. Acad. Sci. U. S. A. 113, 13630–13635.
Wang, Y.Y., Zhang, F., Li, Z.Q., Tan, H.B., Xu, H.B., Ren, J.Y., Zhao, J., Du, W., Sun, Y., 2017. Enhanced hydrophobicity and volatility of submicron aerosols under severe emission control conditions in Beijing. Atmos. Chem. Phys. 17, 5239–5251.
Wehner, B., Philippin, S., Wiedensohler, A., Scheer, V., Vogt, R., 2004. Variability of non-volatile fractions of atmospheric aerosol particles with traffic influence. Atmos. Environ. 38, 6081–6090.
Wehner, B., Berghof, M., Cheng, Y.F., Achtert, P., Birmili, W., Nowak, A., Wiedensohler, A., Garland, R.M., Poschl, U., Hu, M., Zhu, T., 2009. Mixing state of nonvolatile aerosol particle fractions and comparison with light absorption in the polluted Beijing region. J. Geophys. Res.-Atmos. 114.
Xie, Y.Y., Ye, X.N., Ma, Z., Tao, Y., Wang, R.Y., Zhang, C., Yang, X., Chen, J.M., Chen, H., 2017. Insight into winter haze formation mechanisms based on aerosol hygroscopicity and effective density measurements. Atmos. Chem. Phys. 17, 7277–7290.
Ye, X.N., Chen, T.Y., Hu, D.W., Yang, X., Chen, J.M., Zhang, R.Y., Khakuziv, A.F., Wang, L., 2009. A multifunctional HTDMA system with a robust temperature control. Adv. Atmos. Sci. 26, 1235–1240.
Zhang, R.Y., Khalizov, A.F., Pagels, J., Zhang, D., Xue, H.X., McMurry, P.H., 2008. Variability in morphology, hygroscopicity, and optical properties of soot aerosols during atmospheric processing. Proc. Natl. Acad. Sci. U. S. A. 105, 10291–10296.
Zhang, Y.L., Huang, R.J., El Haddad, I., Ho, K.F., Cao, J.J., Han, Y., Zotter, P., Bozzetti, C., Daellenbach, K.R., Canonaco, F., Slowik, J.G., Salazar, G., Schwikowski, M., Schnelle-Kreis, J., Abbaszade, G., Zimmermann, R., Baltensperger, U., Prevot, A.S.H., Szidat, S., 2015. Fossil vs. non-fossil sources of fine carbonaceous aerosols in four Chinese cities during the extreme winter haze episode of 2013. Atmos. Chem. Phys. 15, 1299–1312.
Zuberi, B., Johnson, K.S., Aleks, G.K., Molina, L.T., Laskin, A., 2005. Hydrophilic properties of aged soot. Geophys. Res. Lett. 32.